

## THE HYDROGEN EPOCH OF REIONIZATION ARRAY DISH I: BEAM PATTERN MEASUREMENTS AND SCIENCE IMPLICATIONS

ABRAHAM R. NEBEN<sup>1</sup>, AARON EWALL-WICE<sup>1</sup>, NIPANJANA PATRA<sup>2</sup>, NITHYANANDAN THYAGARAJAN<sup>3</sup>, JAMES E. AGUIRRE<sup>4</sup>, ZAKI S. ALI<sup>2</sup>, JUDD BOWMAN<sup>3</sup> CARINA CHENG<sup>2</sup>, DAVID R. DEBOER<sup>2</sup> JACQUELINE N. HEWITT<sup>2</sup>, AARON PARSONS<sup>2</sup>

<sup>1</sup>MIT Kavli Institute, Massachusetts Institute of Technology, Cambridge, MA, 02139 USA

<sup>2</sup>Dept. of Astronomy, University of California, Berkeley, CA, USA

<sup>3</sup>Arizona State University, School of Earth and Space Exploration, Tempe, AZ 85287, USA and

<sup>4</sup>Dept. of Physics and Astronomy, University of Pennsylvania, Philadelphia, PA

*Draft version December 22, 2015*

### ABSTRACT

THIS WILL NEED TO BE REWRITTEN We deploy the 137 MHz ORBCOMM beam mapping system of Neben et al. (2015a) at the site of the HERA prototype at NRAO–Green Bank. This technique measures the beam of an antenna-under-test relative to that of a well-modeled reference antenna. We characterize environmental systematics such as reflections and multipath effects by comparing the measured beams of different reference antennas, then measure the beam pattern of the east-most HERA dish as a function of feed height over the dish surface. With the feed at the nominal focus of 4.5 m over the dish surface, the collecting area is observed to be 68.5 m<sup>2</sup>, agreeing with simulations. We also simulate delay spectra on baselines of different lengths and orientations at different LSTs for measured and model beams, and quantify the severity of and uncertainties in the delay space horizon brightening termed the “pitchfork effect” by Thyagarajan et al. (2015a). Future measurements will study the dish beam in the presence of adjacent dishes, quantifying levels of cross-talk and cross-coupling.

*Subject headings:* instrumentation: interferometers — techniques: interferometric — cosmology: observations — dark ages, reionization, first stars

### 1. INTRODUCTION

A new generation of low frequency radio telescopes is coming online with the goal of probing redshifted 21 cm emission from the Cosmic Dawn. These observations will complement indirect probes of the Dark Ages and Epoch of Reionization such as quasar sightlines, deep galaxy surveys, and the CMB optical depth which leave the reionization history of the universe only loosely constrained. Sensitivity and foreground removal are the main challenges in 21 cm observations, as the expected cosmological signal is 4–5 orders of magnitude fainter than Galactic and extragalactic foregrounds. Radio interferometers such as the MWA (Tingay et al. 2013), PAPER (Ali et al. 2015b), GMRT (Paciga et al. 2011), and LOFAR (van Haarlem et al. 2013) are seeking a first detection of cosmological 21 cm emission in power spectrum measurements, where the smooth frequency evolution of the foreground emission distinguishes itself from the spectrally jagged cosmological signal whose frequency dimension is a redshift axis probing the inhomogenous reionizing universe.

It was initially thought that the foreground emission would be confined to the lowest few line of sight Fourier modes, however it was later realized that the spectral structure of the interferometer’s point spread function smears foreground power into a “wedge”-shaped region in  $(k_{\perp}, k_{\parallel})$  Fourier space. The complement of this corrupted region is known as the “EOR Window”. Here  $(k_{\perp}, k_{\parallel})$  represent spatial modes perpendicular and parallel to the line of sight. This effect is straightforward to understand for a single baseline which measures the sky intensity weighted by the complex sky fringe  $e^{i\vec{k}\cdot\vec{b}}$ ,

where  $\vec{k} = \vec{k}(\theta, \phi)$  is the wave vector of the incident radiation and  $\vec{b}$  is the baseline vector in meters. A source at zenith has  $\vec{k} \perp \vec{b}$ , and so appears in the visibility without any apparent frequency dependence; however the visibility for a source near the horizon in line with the baseline is maximally frequency dependent, and proportional to  $e^{2\pi i fb/c}$ .

Thus sources at different positions relative to the baseline vector manifest different frequency structure despite their intrinsically smooth spectra, but are geometrically limited by the baseline length so that maximum affected  $k_{\parallel}$  mode is proportional to the baseline length, and thus to  $k_{\perp}$ . It is convenient to phrase this description in terms of the delay in radiation arrival at the baseline’s two antennas,  $\tau$ , where  $\tau_{\max} = b/c$ . The interpretation is thus that sources at low delay have little frequency structure, while those near  $\tau = \tau_{\max}$  acquire the maximum frequency structure given the baseline length.

That sources acquire frequency dependence commensurate with their position in the sky tells us already that the primary beam strongly affects the apparent frequency dependence of the foregrounds. The high delay regions of the sky lie near the horizon while low delay regions lie closer to zenith and also perpendicular to the baseline vector. Thyagarajan et al. (2015a) simulate the foreground contamination seen with a dipole beam, a phased array of simple dipoles, and a Airy dish, and find that the latter suffers minimal foreground contamination into of nonzero  $k_{\parallel}$  mode due to its narrow main lobe and minimal sidelobe levels. To be sure, all are subject to the same geometric limits on foreground frequency-dependence, the wedge, but the emission from high delay is better suppressed using the Airy dish leaving much of

the wedge effectively empty.

In principle, it is irrelevant how empty or full the wedge is of foreground power as it is perfectly contained in it, however the finite bandwidth and imperfect frequency bandpass of real instruments smear power beyond the geometrical edge of the wedge into the EOR window. Sources at higher delay appear closest to the edge of the wedge, and thus are most at risk of leaking into the EOR window due to these effects. In fact, Thyagarajan et al. (2015a); Thyagarajan et al. (2015b) observe that while naively we might expect minimal emission at the very edge of the wedge because typical near-horizon beam responses are so small, two effects cause a relative brightening of emission at those maximal delays after the decline away from zero delay, creating a characteristic “pitch-fork” shape. This horizon brightening is caused by the large solid angle subtended by the near-horizon regions of the sky, and the apparent shortening of baselines when viewed on axis at these elevations. This second effect makes intermediate length baselines sensitive to the very bright diffuse emission they would not otherwise be sensitive due to its very weak coupling to longer baselines. Together, these effects can over the decline in beam sensitivity near the horizon. All these considerations highlight the antenna beam as a critical design parameter for 21 cm observatories

This is the first paper in a series of four papers detailing the HERA element. We focus on the angular response of the dish and its implications for power spectrum measurements. The three companion papers present reflectometry measurements (Patra et al., submitted) and simulations (Ewall-Wice et al., submitted) of the dish frequency response, as well as detailed foreground simulations for HERA (Thyagarajan et al., submitted). A general description to the design of the HERA experiment from an engineering point of view is given by DeBoer et al. (submitted). In essence, we require a large collecting area for sensitivity and minimal sidelobes and horizon response without incurring the large cost per collecting area of very large dishes. A dish is preferred to a large phased array as it has fewer degrees of freedom and reduced potential of antenna-to-antenna variation (Neben et al. 2015b, submitted). These factors naturally lead to a 14 m diameter parabolic dish with a dipole feed suspended at prime focus. The 352 dishes are positioned in a compact, hexagonal array permitting redundant baseline calibration and coherent integration in  $\vec{k}$  space (Zheng et al. 2014; Ali et al. 2015b).

In this paper we first characterize the angular response of a prototype HERA dish at the National Radio Astronomy Observatory–Green Bank. We use the technique data acquisition system of Neben et al. (2015a) to measure the 137 MHz beam pattern using the ORBCOMM satellite constellation, allowing beam measurements down to roughly -35 dB from zenith, corresponding to an elevation roughly 30°. We perform these measurements with the feed suspended at different heights above the dish, and compare the observed power patterns and collecting areas with models. We consider the science implications of these results by simulating visibilities with these beam models, testing different models of the sub-30° elevation beam response unprobed by our measurements. We run these simulations for baselines of

different lengths and orientations at different local sidereal times to study under when the leakage out of the wedge is significant, and what regions of the EOR window are affected.

In detail, we discuss the electromagnetic design and modeling of the dish in Section 3. We present the experimental setup of the beam mapping experiments and discuss their systematics, then review the ORBCOMM beam measurement system, in Section 3. We present our power pattern measurements in Section 5. We conclude with discussion in Section 6.

## 2. DISH DESIGN AND MODELING

### 2.1. Design of the HERA Dish



FIG. 1.— Aerial photograph of the two reference dipoles deployed in Galford Meadow at the National Radio Astronomy Observatory–Green Bank 100 m south of the HERA dish.



FIG. 2.— Aerial photograph of the two reference dipoles deployed in Galford Meadow at the National Radio Astronomy Observatory–Green Bank 100 m south of the HERA dish.

The 14 m HERA dish design is a departure from the large N–small D approach used by 21 cm observatories like PAPER and the MWA. Both observatories are actively pursuing power spectrum analyses using several

year data runs, but the sheer data volume makes characterization and removal of systematics, as well as repeated or complimentary analyses, challenging. A larger element was chosen for HERA primarily to economize data volume. The natural consequence of a larger antenna aperture is a smaller field of view, but this is a small effect for 21 cm power spectrum analyses as our leverage on  $k$  modes in the spherically averaged power spectrum comes primarily from  $k_{\parallel}$  modes along the line of sight (in the frequency dimension).

However, such a turn from small, simpler antenna elements to larger, more complex dishes with suspended feeds must be done judiciously, lest the chromatic antenna response smear otherwise smooth spectrum foreground power into cosmological signal modes. For this reason the dish design was carefully optimized for a foreground avoidance-based power spectrum spectrum analysis, as detailed by Parsons & DeBoer (2015) and discussed in the larger engineering context of HERA by DeBoer et al (in prep).

We summarize here the logic leading to a 14 m dish with  $f/D \approx 0.32$ . As discussed above, it is useful to think in delay-space, where a source ideally appears as a delta function at the delay corresponding to the difference in light travel time to two antennas in a baseline. In a real instrument, finite bandwidth and intrinsic source spectral structure (synchrotron sources typically have  $I \propto f^{-0.85}$ ) smear foreground power over a kernel as wide as  $\sim 60$  ns. All antennas have some frequency structure as well, though dipole-like elements such as sleeved dipoles and bowties may be made relative frequency independent over wide bands. Suspension of a feed over a dish introduces frequency structure directly due to time domain reflections between the dish and feed. We optimize the HERA dish so this frequency structure extends no farther into delay space than the 60 ns intrinsic width of foregrounds. This was accomplished first through numerical modeling of the beam pattern with a PAPER dipole suspended over the dish aperture, and resulted in a maximum efficiency of 73% with  $f/d \approx 0.32$ . From there, using realistic estimates of reflection loss, a 14 m dish was observed to have the property that the signal received at the feed after two bounces (round trips between the dish and feed) is above -60 dB but contained in the wedge, but all higher order reflections in the EOR window are below -60 dB, and thus an order of magnitude smaller than the expected cosmological signal.

In reality, the HERA dishes are somewhat more complicated than these simple considerations imply, and part of the purpose of the beam measurements presented in this paper is to characterize their *in situ* beam patterns. The dish is fabricated out of low cost construction materials with an expected lifetime of  $\sim 5$  years, sufficient to detect the 21 cm power spectrum to high significance before the Square Kilometer Array builds a longer lasting instrument to more fully characterize the Epoch of Reionization with imaging. The feed consists of a sleeved dipole, suspended in a cage structure from three ropes attaching to telephone poles spaced around the dish. The dipole is mounted on a XX m mast over a XX m diameter backplane surrounded by a XX m long cylindrical “skirt” designed to reduce cross coupling with adjacent elements by narrowing the feed’s response. The dish

surface consists of 12 wire mesh strips secured to 60 mm PVC pipes forming the dish skeleton. A spar at 2.4 m elevation is added to ensure approximately parabolic shape. Note that we refer to this design as a *faceted parabola* given that the dish surface between PVC spars is not curved, though our design ensures the Ruze loss is at the percent level. A door is engineered into one of these mesh strips to facilitate feed maintenance.

This work presents beam pattern measurements to verify the capabilities of this new dish, in particular the position of the dish focus, the shape of the main lobe, the magnitude of the dish sidelobes, the degree of beam symmetry, the actual dish/feed efficiency (i.e., collecting area), and the expected level of antenna-to-antenna variation.

## 2.2. Dish Modeling

ASK DAVE OR RICH TO WRITE A ONE OR TWO PARAGRAPH SUMMARY OF THE ELECTROMAGNETIC DISH SIMULATIONS

## 3. EXPERIMENTAL SETUP

### 3.1. HERA–Green Bank: A three-element prototype array

A 3-element HERA engineering prototype array is being constructed at the National Radio Astronomy Observatory–Green Bank. We performed the beam measurements presented in this work on the first of these to be constructed, future work will characterize how its *in-situ* beam in the presence of the other two dishes once they are constructed. Figure ?? shows the west-most HERA dish next to two planned dishes in Galford Meadow. The two reference antennas 100 m are positioned due south with a 100 m separation, and the Green Bank Telescope  $\sim 1$  km northwest of the dish. The data acquisition system is installed in the hut labeled “Launch point” on the image.

Note that unlike the full HERA site in the Karoo Desert Radio Astronomy Reserve in South Africa, the Green Bank site has obstructions such as trees and foothills, as well as moist ground with possibly non-uniform properties. All these will contribute to variation of the *in-situ* reference antenna relative to the electromagnetic model. We will discuss below how we quantify these systematics with “null experiments” which compare the beams of the two reference antennas.

### 3.2. ORBCOMM Beam Mapping System Review

We briefly review the beam mapping system detailed by Neben et al. (2015a), then discuss application of system to the prototype HERA array at NRAO–Green Bank. The system takes advantage of the 137 MHz communications satellites operated by ORBCOMM Inc. as bright point sources which, by virtue of their number ( $\sim 30$ ), short orbital periods ( $\sim 90$  minutes), and orbital precession cover 65% of the visible sky in just a few days. The coverage is limited by the fact that the satellites’ orbital inclinations are all less than  $45^\circ$ .

In contrast to celestial source beam measurements, though, where the flux may be assumed constant over the timescale of the measurement, satellite fluxes can vary rapidly due to varying distance, orientation, and transmission power. To correct for this, we measure the

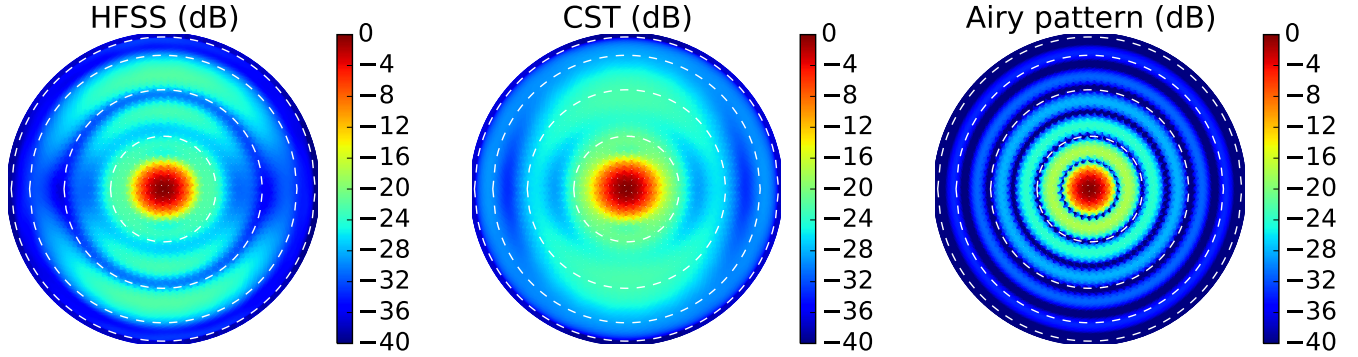


FIG. 3.— Simulated delay spectra for the GSM and point sources at  $0^\circ$  (top pair) and  $60^\circ$  (bottom pair) LST for EW baselines of length 14 m (left pair) and 42 m (right pair). The beams are assumed constant over frequency.

satellite flux in each ground polarization (EW and NS) using a simple, well-modeled reference antenna. Comparison of this measured power with that observed in the Antenna-Under-Test (AUT) gives the AUT beam response in the direction of the satellite. An equivalent interpretation is that the power ratio between the AUT and the reference antenna gives the relative beam response in the satellite direction, and multiplication by the reference antenna model yields the desired AUT response. As discussed in Neben et al. (2015a), despite the fact that satellite signals are generally polarized, this procedure.

In detail, we measure the dual-polarization RMS powers for each antenna in 512 2 kHz bands across the 137–138 MHz band. Each channel power is averaged over  $\sim 0.2$  sec. There are 0–3 satellites above the horizon at any given time transmitting on different  $\sim 15$  kHz wide sub-bands in 137–138 MHz. By observing at many different frequencies, we probe the beam response in all these directions simultaneously. We compute the satellite positions using the orbital elements published by Celestrak<sup>1</sup> and the orbital integrator predict<sup>2</sup>. However, the satellite frequencies vary occasionally to avoid interference within the constellation. Zheng et al. (2014) use interferometric phases to identify and exclude times when multiple satellites are in view. As our data acquisition system makes only total power measurements, we instead use an ORBCOMM interface box (typically supplied to commercial users of the network) to sync with passing satellites and record their identifier and transmission frequency.

In this way, beam measurements are built up along satellite tracks over the course of several days of integration, yielding typically 200–300 satellite pass. Each pass is processed separately to identify and exclude times of low signal-to-background when the satellite is low in the sky or in the off state of a pulsing sequence. At those times, the satellite flux no longer dominates over that of the diffuse Galactic background, and a power measurement no longer probes the response in the satellite direction. The beam measurements are then gridded in horizontal coordinates in HEALPix with a resolution of  $1.8^\circ$  ( $\text{nsidel} = 32$ ). As a last quality control step to reject errant beam measurements due to RFI, for instance, we keep only the central 90% of  $\sim 50$  measured beam values

in each HEALPix cell.

### 3.3. Assessing Experimental Systematics

As in Neben et al. (2015a), we assess systematics using a “null experiment” in which we use a second reference dipole as the antenna-under-test (AUT). Taking the ratio of its measured power pattern with the model beam pattern amounts to a ratio of the raw power responses received by the two antennas. This test thus probes the level of environmental systematics (i.e., reflections and varying ground properties) and antenna fabrication imperfections which affect each antenna differently. This is not a probe of modeling imperfections common to both antennas, but we expect such errors to be subdominant as the physical properties of the antenna are easier to characterize, and thus simulate, than local environmental effects.

We run three null experiments with the reference dipoles deployed varying distances from the HERA dish and from each other.

- **null1:** reference dipoles deployed 50 m apart on a NS line, 50 m south of the HERA dish
- **null3:** same as **null1** but with the south-most reference antenna moved 5 m west
- **null4:** same as **null1** but with 100 m separation between both reference antennas and from the dish

Figure ?? shows the results from the **null1** experiment in the form of the ratio of the power responses of the two antennas (top panel), and slices through the E and H planes of the reconstructed power patterns (bottom panel). We collected roughly 100 satellite passes. Systematics at the few percent level are observed in within  $20^\circ$  of zenith, and at the  $\sim 10\%$  level farther out.

The magnitude of these systematics is comparable to those observed in the two other null experiments (Figures ?? and ??), and their angular distribution appears largely unchanged. This suggests that the reference dipoles differ both due to varying environmental properties and perhaps intrinsic differences. In any case, these fractional errors propagate directly into the measured beam-patterns of our subsequent feed and dish measurements.

## 4. DISH MEASUREMENTS

### 4.1. Power pattern measurements

<sup>1</sup> <http://www.celestrak.com/NORAD/elements/orbcomm.txt>

<sup>2</sup> <http://www.qsl.net/kd2bd/predict.html>

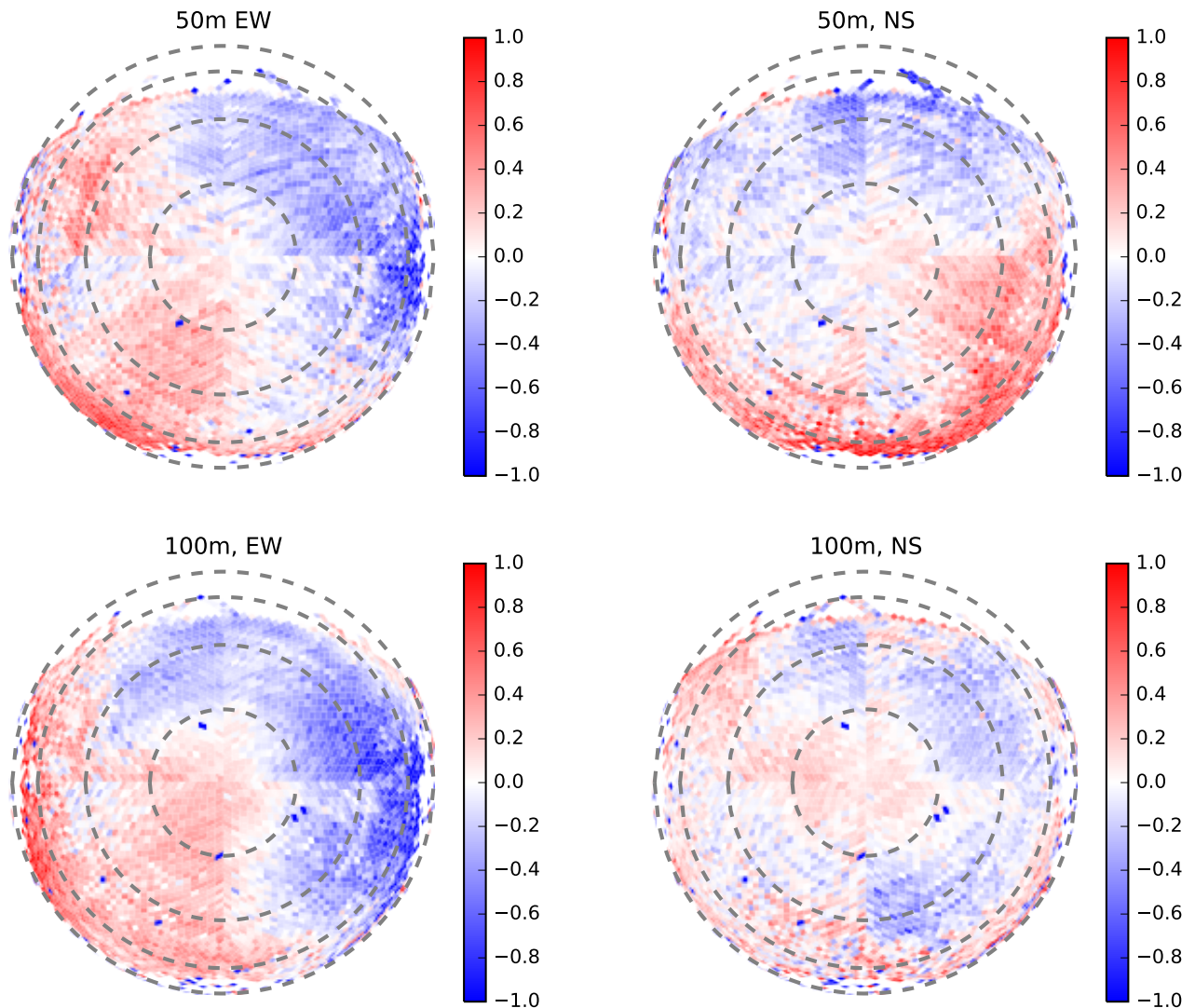


FIG. 4.— null experiment beam ratio plots

Having verified the feed power pattern, we deployed feed over the dish and proceed with dish measurements. We measure the power pattern with the feed at four different heights, 4 m, 4.5 m, 5 m, and 5.3 m, chosen to probe around the nominal focus of 4.5 m (the nominal beam) and up to the maximum height of 5.3 m allowed by pole height and rope stresses. Heights are measured from the dish surface to the feed backplane.

Inspecting the E and H plane slices through the measured beams (bottom panels) in Figures ??, ??, ??, ??, ??, we generally see the main lobe narrow and the sidelobe level decrease. The improvement is also seen in the yellow and red main lobe in the beam maps (top panels) which narrow and approach the expected orientations: the EW (NS) main lobe is elongated in the NS (EW) direction. The last lift produced the smallest change in the beam suggesting it is quite near the best focus.

The sky coverage in these dish measurements extends out to typically  $\theta \sim 50 - 60^\circ$ . Beyond that the ORB-COMM flux is sufficiently attenuated relative to diffuse galactic emission that a power ratio measurement between the two antennas is no longer a clean probe of their gains in the direction of the satellite. At these zenith angles, the beam sidelobes are roughly -30 dB, and seem to be trending downward at the edge of the measured region.

In order to compute beam collecting areas and assess foreground leakage we require a beam covering the entire visible sky. For each measured dish beam, we interpolate over the unmeasured cells at  $\theta \lesssim 60$ , then extrapolate outward to the horizon. This amounts to a smooth continuation of the beam response at the same  $\sim -30$  dB level suggested by the fringes of our measurements. We take this as a first possible model of the full sky dish beam, and construct a second with a gaussian cutoff at  $\theta = 60^\circ$  with  $\sigma = 2.5^\circ$ , the pair of which span the space of likely horizon responses. This procedure is depicted in Figure ?? where we plot the measured nominal focus beam, the beam after interpolation and extrapolation, and the beam after applying the gaussian cutoff. Figure ?? shows the interpolated/extrapolated beam and the beam with the cutoff along with various models to illustrate the different horizon responses more clearly.

To illustrate the results of these smoothing operations we plot slices through the nominal focus dish beam along with the three model beams discussed in Sec. 2.2. The H (E) plane slice of the main lobe is shown at the top (bottom). The plots in the left side zoom in on the main lobe, while those on the right show a zoomed out view of the entire sky pattern.

#### 4.2. Collecting Area

The collecting area of the antenna is related to the power pattern by the ratio of the beam gain to its beam-weighted solid angle as

$$A = \frac{\lambda^2 B(0, 0)}{\int B(\theta, \phi) d\Omega} \quad (1)$$

We evaluate the collecting area for four of the beams discussed above and present the numbers in Table 1. We are unable to quantify the collecting area of the beam from Dave's simulation because it was run at too coarse an angular resolution. For the measured beams, we compute

the collecting area using the interpolated/extrapolated beams with and without the gaussian cutoff at  $\theta = 60^\circ$ .

TABLE 1  
COLLECTING AREA ( $\text{m}^2$ ) OF MEASURED 137 MHZ BEAMS AND CORRESPONDING POWER SPECTRUM SNR FOR HERA-127.

Beam	$A_{\text{eff}}$ ( $\text{m}^2$ )	SNR (pess, mod, opt)
Airy pattern	155	9.1, 11.0, 37.2
Measured, feed at 5.3 m	97.9	8.2, 8.3, 29.2
Measured, feed at 5 m	82.6	6.8, 6.9, 26.5
Measured, feed at 4.5 m	73.6	6.4, 6.5, 24.8

By definition, the Airy pattern has the largest collecting area equal to the dish cross section. The others model a realistic feed with a hanging screen (the skirt or "kilt"), effectively tapering the dish response to radiation received from its fringes to mitigate cross-coupling and crosstalk between adjacent dishes. As expected, raising the height of the feed increases the illuminated area of the dish, and thus, its collecting area. As expected, the measured collecting area matches that of the CST model at the nominal focus height of 4.5 m.

Why does the collecting area increase as the feed is raised over the nominal focus? There are two computing effects here: (1) the reflected radiation is less well focused above the feed, decreasing the response; and (2) the tapered feed sees a larger dish as it is raised, allowing more radiation to reach the dipole as opposed to reflecting off the skirt. These data suggest that the second effect wins. Of course the reason for the skirt is to taper the feed beam in order to mitigate cross-talk and cross-coupling between the dishes. A larger collecting area may not be worth it in exchange for exacerbating these concerns.

#### 5. FOREGROUND LEAKAGE AND RESIDUALS

We assess the level of foreground leakage into the EOR window due to beam shape, baseline length, and LST. In particular, we built on the study of Thyagarajan et al. (2015a) of the impact of beam shape and horizon response on foreground spectral structure and containment in the wedge.

We simulate delay spectra for several model and measured beams on different baseline lengths for different LSTs and baseline orientations. All these factors affect the level of emission horizon brightening in delay space, the "pitchfork" effect, and the level of foreground leakage. We assume a constant beam pattern over that band, with leakage due only to the finite bandwidth and choice of window function. Actual frequency structure imprinted onto the foregrounds by variation of the beam angular pattern or overall gain with frequency (Patra et al.)

We begin by simulating visibilities over a 20 MHz bandwidth with 400 kHz resolution centered on 137 MHz on two different baselines for two model beams (airy, and CST sim) and two measured beams (measured nominal focus beam, and measured nominal focus beam with  $60^\circ$  cutoff). We use the short and maximally redundant 14 m baseline, most useful for delay spectrum analysis, as well as a longer 42 m baseline, more useful for imaging analysis. From these frequency-sequenced visibilities we calculate the delay spectrum (Parsons et al. 2012) using the Blackman-Harris window following Thyagarajan

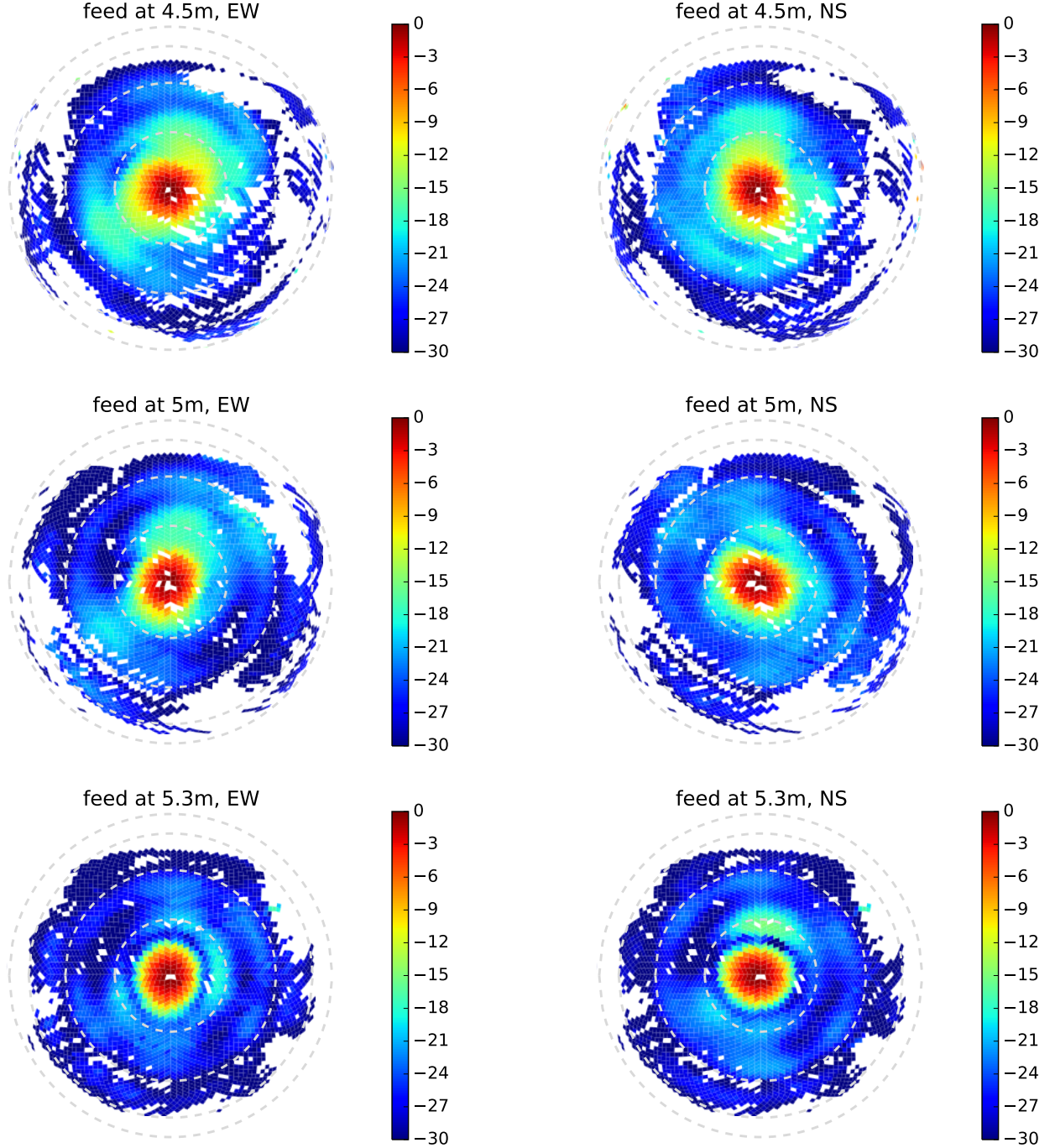


FIG. 5.— null experiment beam ratio plots

et al. (2015a). This window reduces the noise equivalent bandwidth to 10 MHz, corresponding to  $\Delta z \sim 0.5$ , beyond which evolution of the cosmological signal become significant. Larger bandwidths, though, are useful for foreground estimation and delay-space deconvolution (Parsons & Backer 2009; Parsons et al. 2014; Ali et al. 2015a). With this caveat, our simulated delay spectra show the worst case scenario, quantifying the level of foreground isolation without estimation and deconvolution.

Our sky model is comprised of a deep MWA point source survey within  $20^\circ$  of R.A.(J2000) =  $0^{\text{h}} 0^{\text{m}} 0^{\text{s}}$  and

decl.(J2000) =  $-30^\circ 0' 0''$  (Carroll et al., in prep.), the shallower but wider MWA commissioning point source survey(Hurley-Walker et al. 2014), the Culgoora catalog(Slee 1995), and the Global Sky Model of Galactic radio emission (de Oliveira-Costa et al. 2008).

Figure 3 shows the delay spectra at  $0^\circ$  (top pair) and  $60^\circ$  (bottom pair) LST for 14 m (left pair) and 42 m (right pair) EW baselines. For reference we plot a 1D model 21 m power spectrum for  $z \sim 8$  from Mesinger et al. (2011). Consider first the  $0^\circ$  LST plots where the Galactic disk has nearly, but not completely set. The effect of horizon response is most visible on the longer 42 m

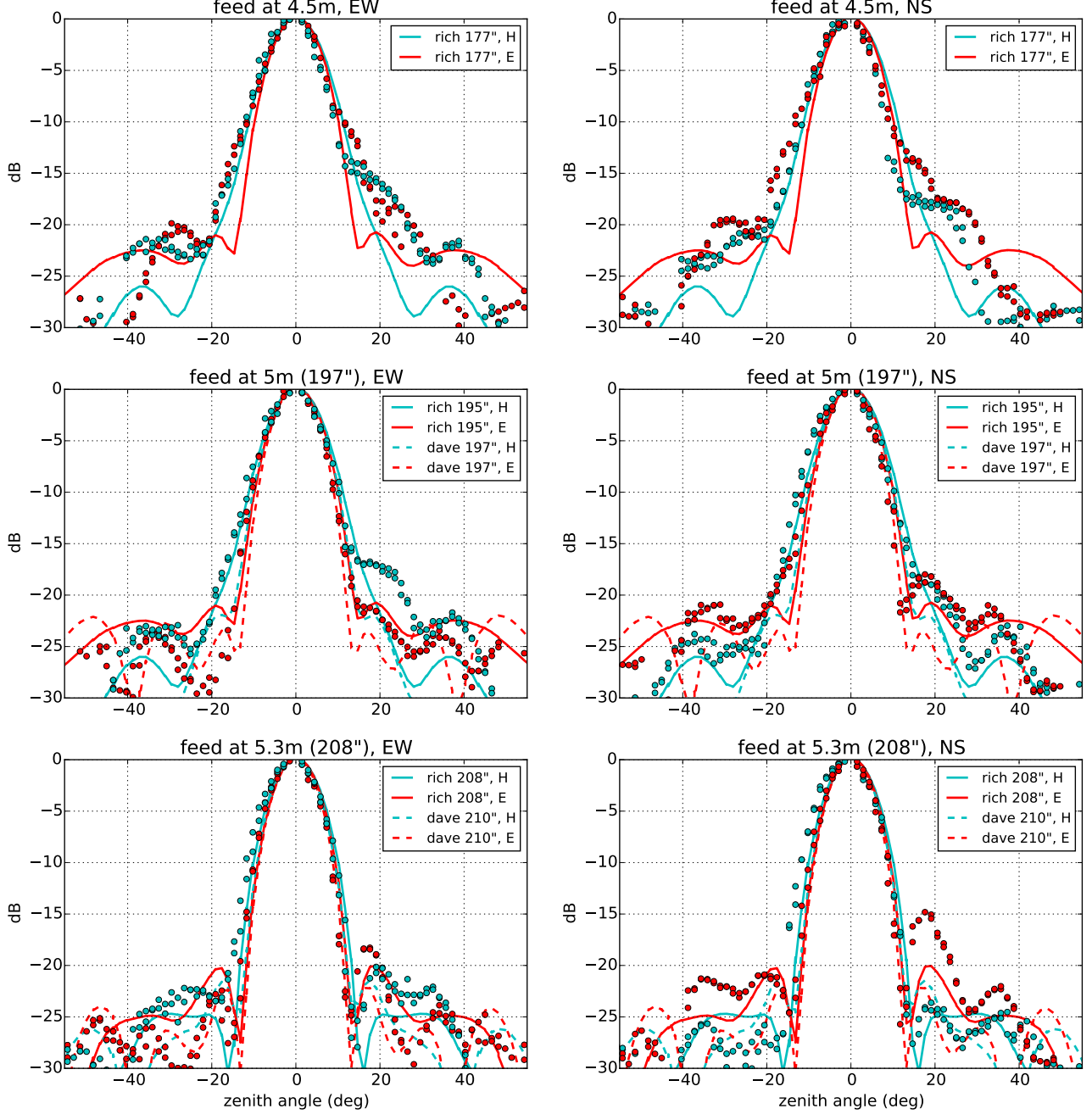


FIG. 6.— null experiment beam ratio plots

baseline where the measured beam (red) and CST model (yellow), both show significant brightening at the horizon delays (vertical black lines) due to roughly -30 dB beam response near the horizon, as discussed by Thyagarajan et al. (2015a,a). In contrast, the airy model (black) and measured beam with cutoff (blue) show no significant brightening at the horizon, where they appear still to be dominated by the wings of the delay PSF from the emission closer to zero delay.

We also plot (green dashed line) the delay spectrum after subtracting the visibilities computed with the  $\theta \sim 60^\circ$  cutoff measured beam from those using the full measured beam. This curve may be interpreted as the uncertainty in the “pitchfork” horizon brightening due to uncertainty

in the beam horizon response, or equivalently as the delay spectrum residual foregrounds after subtracting foregrounds in the well modeled region of the sky (Neben et al. 2015b, submitted). By construction, this subtraction leaves emission from the highest delay regions of the sky (near the horizon on opposite sides of the baseline), but also leaves some low delay emission on opposite sides of a line perpendicular to the baseline. However, this additional low delay emission near the horizon gets drowned out by that from near zenith where the beam is substantially stronger.

On the shorter 14 m baseline, the horizon brightening is smaller because there is roughly an order of magnitude more emission at zero delay, whose thereby stronger de-

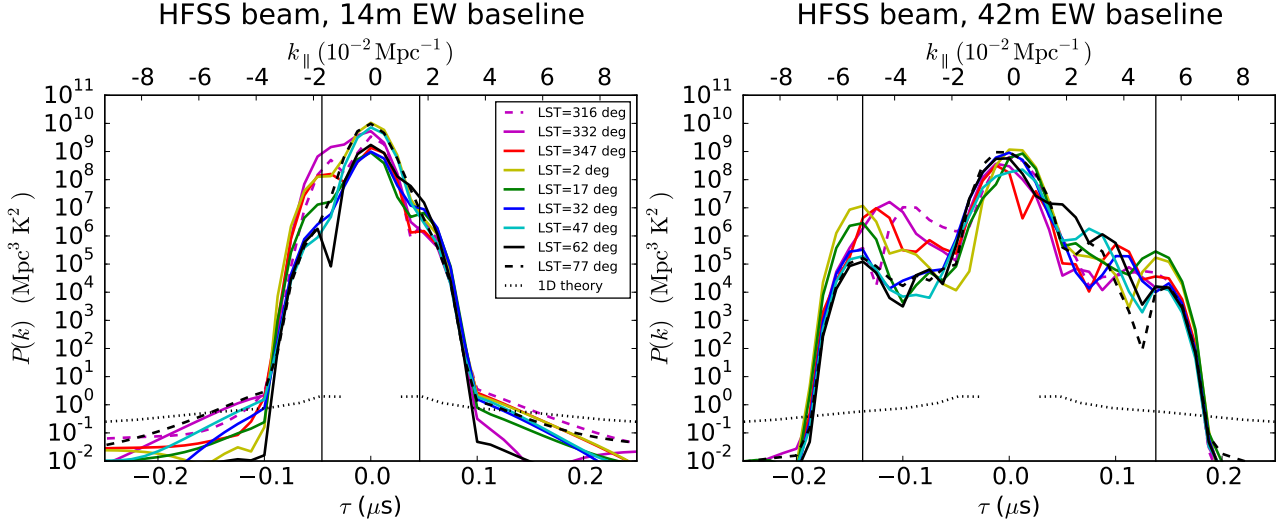


FIG. 7.— Simulated delay spectra for the GSM and point sources at  $0^\circ$  (top pair) and  $60^\circ$  (bottom pair) LST for EW baselines of length 14 m (left pair) and 42 m (right pair). The beams are assumed constant over frequency.

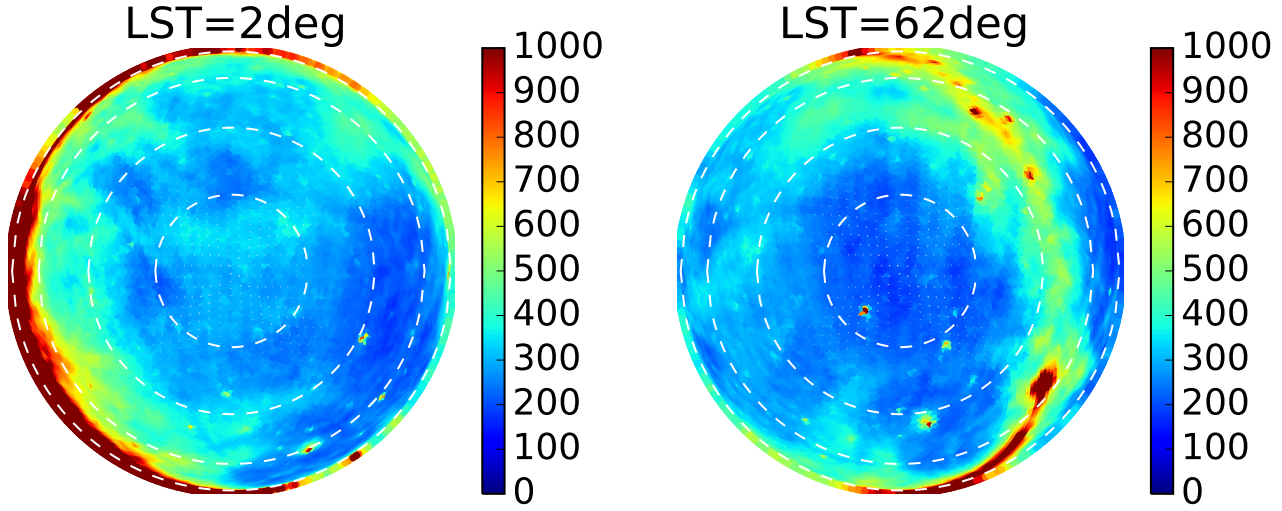


FIG. 8.— Simulated delay spectra for the GSM and point sources at  $0^\circ$  (top pair) and  $60^\circ$  (bottom pair) LST for EW baselines of length 14 m (left pair) and 42 m (right pair). The beams are assumed constant over frequency.

lay wings, which are also relatively wider compared to the narrower foreground wedge, cover up much of the edge brightening. At  $60^\circ$  LST, effect of horizon response is much smaller as the Galactic disk is now entirely below the horizon.

The level of leakage depends also on baseline orientation which sets which directions on the sky map to large delays. Figure ?? shows the delay spectra at  $0^\circ$  LST on 14 m NE (top pair) and SE (bottom pair) baselines.

Both show increased edge brightening compared to the 14 m EW baseline. Thyagarajan et al. (2015a) proposes to identify through modeling the baselines most susceptible to this edge brightening at any given time, and simply exclude them from the power spectrum analysis.

## 6. DISCUSSION

add stuff here

## REFERENCES

- Ali, Z. S., et al. 2015a, ApJ, 809, 61  
 —. 2015b, ArXiv e-prints  
 de Oliveira-Costa, A., Tegmark, M., Gaensler, B. M., Jonas, J., Landecker, T. L., & Reich, P. 2008, MNRAS, 388, 247  
 Hurley-Walker, N., et al. 2014, PASA, 31, 45  
 Mesinger, A., Furlanetto, S., & Cen, R. 2011, MNRAS, 411, 955  
 Neben, A. R., et al. 2015a, Radio Science, 50, 614  
 Paciga, G., et al. 2011, Monthly Notices of the Royal Astronomical Society, 413, 1174  
 Parsons, A. R., & Backer, D. C. 2009, AJ, 138, 219  
 Parsons, A. R., & DeBoer, D. R. 2015, Configuration of the HERA Element, Tech. Rep. 5, HERA Memo Series  
 Parsons, A. R., Pober, J. C., Aguirre, J. E., Carilli, C. L., Jacobs, D. C., & Moore, D. F. 2012, ApJ, 756, 165  
 Parsons, A. R., et al. 2014, ApJ, 788, 106  
 Slee, O. B. 1995, Australian Journal of Physics, 48, 143  
 Thyagarajan, N., et al. 2015a, ApJ, 804, 14  
 Thyagarajan, N., et al. 2015b, ApJ, 807, L28  
 Tingay, S. J., et al. 2013, Publications of the Astronomical Society of Australia, 30  
 van Haarlem, M. P., et al. 2013, A&A, 556, A2  
 Zheng, H., et al. 2014, MNRAS, 445, 1084  
 Zheng, H., et al. 2014, Monthly Notices of the Royal Astronomical Society, 445, 1084

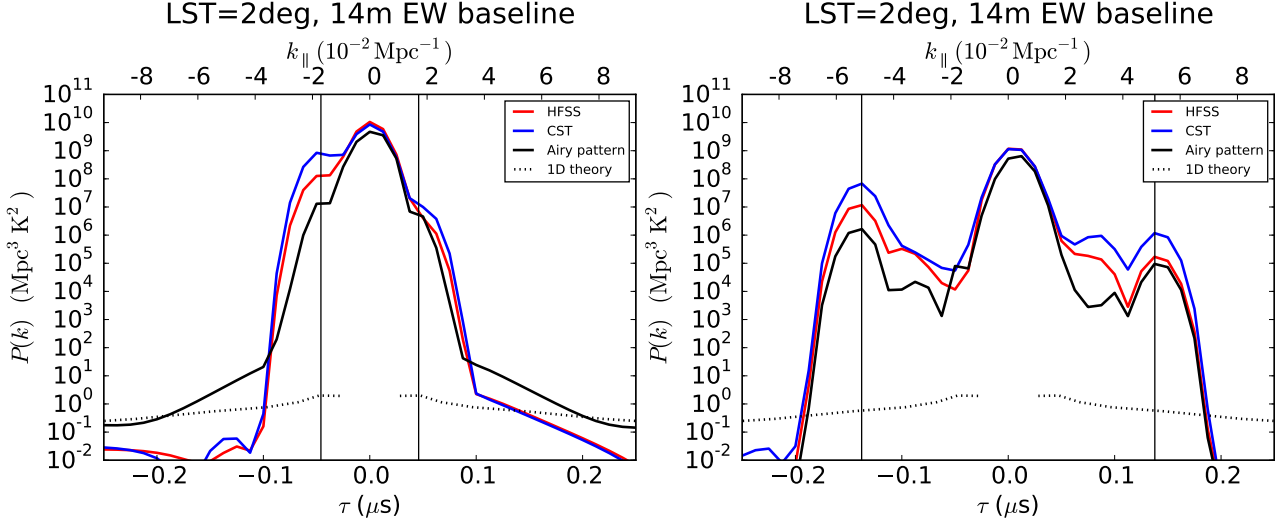


FIG. 9.— Simulated delay spectra for the GSM and point sources at  $0^\circ$  (top pair) and  $60^\circ$  (bottom pair) LST for EW baselines of length 14 m (left pair) and 42 m (right pair). The beams are assumed constant over frequency.

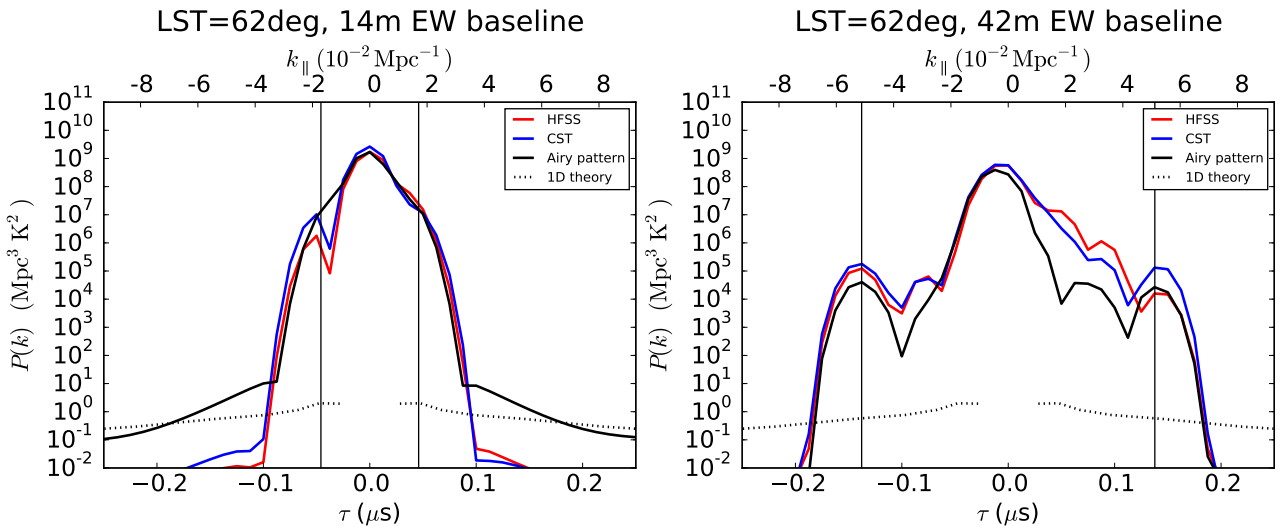


FIG. 10.— Simulated delay spectra for the GSM and point sources at  $0^\circ$  (top pair) and  $60^\circ$  (bottom pair) LST for EW baselines of length 14 m (left pair) and 42 m (right pair). The beams are assumed constant over frequency.